BNL-211848-2019-JAAM

Bi-continuous pattern formation in thin films via solid-state interfacial dealloying studied by multimodal characterization

C. Zhao, X. Huang

To be published in "Materials Horizons"

June 2019

Photon Sciences

Brookhaven National Laboratory

U.S. Department of Energy

USDOE Office of Science (SC), Basic Energy Sciences (BES) (SC-22)

Notice: This manuscript has been authored by employees of Brookhaven Science Associates, LLC under Contract No. DE-SC0012704 with the U.S. Department of Energy. The publisher by accepting the manuscript for publication acknowledges that the United States Government retains a non-exclusive, paid-up, irrevocable, world-wide license to publish or reproduce the published form of this manuscript, or allow others to do so, for United States Government purposes.

DISCLAIMER

This report was prepared as an account of work sponsored by an agency of the United States Government. Neither the United States Government nor any agency thereof, nor any of their employees, nor any of their contractors, subcontractors, or their employees, makes any warranty, express or implied, or assumes any legal liability or responsibility for the accuracy, completeness, or any third party's use or the results of such use of any information, apparatus, product, or process disclosed, or represents that its use would not infringe privately owned rights. Reference herein to any specific commercial product, process, or service by trade name, trademark, manufacturer, or otherwise, does not necessarily constitute or imply its endorsement, recommendation, or favoring by the United States Government or any agency thereof or its contractors or subcontractors. The views and opinions of authors expressed herein do not necessarily state or reflect those of the United States Government or any agency thereof.

Bi-continuous Pattern Formation in Thin Films via Solid-State Interfacial Dealloying Studied by Multimodal Characterization

Chonghang Zhao[1], Kim Kisslinger[2], Xiaojing Huang[3], Ming Lu[2], Fernando Camino[2], Cheng-Hung Lin[1], Hanfei Yan[3], Evgeny Nazaretski[3], Yong Chu[3] Bruce Ravel[4], Mingzhao Liu[2], Yu-chen Karen Chen-Wiegart[1,3*]

[1] Department of Materials Science and Chemical Engineering, Stony Brook University, Stony Brook, NY 11794, U.S.A.

[2] Center for Functional Nanomaterials, Brookhaven National Laboratory, Upton, NY 11973, U.S.A.

[3] National Synchrotron Light Source II, Brookhaven National Laboratory, Upton, NY 11973, U.S.A

[4] Materials Measurement Laboratory, National Institute of Standards and Technology, Gaithersburg, MD 20899, U.S.A.

Email: Karen.Chen-Wiegart@stonybrook.edu

Abstract

Bicontinuous-nanostructured materials with three-dimensionally (3D) interconnected morphology offer unique properties and potential applications in catalysis, biomedical sensing and energy storage. The new approach of solid-state interfacial dealloying (SSID) opens a route for fabricating bi-continuous metal-metal composites and porous metals at nano-/meso-scales via a self-organizing process driven by minimizing the system's free energy. Integrating SSID and thin film processing fully can open up a wide range of technological opportunities in designing novel functional materials; to-date, no experimental evidence showed that 3D bi-continuous film can be formed with SSID, owing to the complexity in kinetic mechanisms in thin film geometry and at nano-scales, despite the simple processing strategy in SSID. Here, we demonstrate a fully-interconnected 3D bi-continuous structure can be achieved by this new approach, thin-film-SSID, using Fe-Ni film dealloyed by Mg film. The formation of Fe-Mg_xNi bi-continuous 3D nano-

structure was visualized and characterized via a multi-scale, multi-modal approach, combining electron transmission microscopy with synchrotron X-ray fluorescence nano-tomography and absorption spectroscopy. Phenomena involved with structural formation are discussed. These include surface dewetting, nano-size void formation among metallic ligaments, and interaction with substrate. This work sheds light on the mechanisms of the SSID process, and sets a path for manufacturing of thin-film materials for future nano-structured metallic materials.

Introduction

Dealloying used as a materials-processing method selectively removes one or more components from a parent alloy, while remaining component(s) form a bi-continuous structure. With advantages of retention of precursor structure, self-organizing bi-continuous structure and tunable feature size, dealloying has become one of the most promising methods to fabricate nanoporous structures. Dealloying has been applied to fabrication of a wide range of materials for different applications, such as catalysts[1], fuel cells[2], batteries[3, 4] and radiation damage-resistant materials[5]. The kinetics and mechanisms of the dealloying process have also been studied extensively. Studies on the pattern formation showed a competing mechanism between dissolution and diffusion[6, 7]. Simultaneously, a coarsening process driven by reducing the surface area occurs during the dealloying process; the dynamics of coarsening evolution has been simulated by kinetics Monte Carlo (KMC) and molecular dynamics (MD), providing explanations for the morphological evolution[8, 9]. The characterization and quantification of such complex topologies have also been developed via electron microscopy[10, 11], X-ray microscopy[12-15], and atom probe tomography (APT) methods[16].

Aqueous solution dealloying (ASD) has been the most widely used method for fabrication of nanoporous metals[17]. Recently, dealloying using a metal agent replacing acid or base aqueous solution as dealloying agent, was re-introduced as a novel method to fabricate nanoporous materials. This is based on the difference of mixing enthalpies between elements of precursor alloy and dealloying agent, leading to selective dissolution. Therefore, rather than limited by precursor alloys with sufficient reduction potential difference within the components, a liquid metal dealloying (LMD) method has been applied to fabricate nanoporous materials that are less noble,

such as stainless steel[18], silicon[3], titanium[19], graphite[20]. Their 3D morphological parameters including curvature, porosity and interfacial shape distribution have been quantified using X-ray nano-tomography, with analysis on the morphology difference between dealloying front and a later dealloying stage[21, 22]. Phase field modeling[23, 24] and detailed experimental analysis[25] were conducted to understand the kinetics and the structural evolution during LMD. Although LMD has been successfully applied to fabricate different materials and pioneering studies have been conducted to understand the mechanisms, the relative high fabrication temperature generally generates porous materials with larger ligament and pore size; in addition, the high temperature molten metal liquid environment resulted in difficulties for kinetics studies.

A new method, solid-state interfacial dealloying (SSID), overcomes these disadvantages and has received recent attention. SSID's lower processing temperature enables formation of structures with finer feature sizes than LMD. Meanwhile, it still takes the advantage of using a metal as the dealloying agent to broaden the applications. SSID was first introduced by Wada *et al*. to fabricate nanoporous Fe-Cr alloys[26] and then nanoporous Ti[27]. The design criteria for SSID was analyzed by McCue *et al*. In their studies, they used thin film precursor alloys deposited on thick solid dealloying agent substrates to study influences of volume changes and interdiffusivity of the dealloying agent and the dissolving components on the bi-continuous structures[28].

The previous SSID studies focused mostly on dealloying bulk structures. However, because of the lower reaction temperature, a pore-ligament size gradient was observed in SSID as a result of the simultaneous coarsening during a slower dealloying process.[26] Thus, fabricating bi-continuous structures by SSID in a film geometry can mitigate this challenge by producing a laterally homogeneous nano-structure for certain applications. McCue *et al*. introduced SSID in thin film precursor alloys, while using thick solid dealloying agent substrates.[28] A fully integrated thin film process with both dealloying agent and precursor in thin film form have yet to be demonstrated to form 3D bi-continuous films to widen the applications. Moreover, in previous SSID studies, the dealloying process was conducted at relative high temperatures for a very long time (hours). As a result, limited observation has been made to study the nano-size morphological evolution in SSID, especially at the dealloying interface. In contrast to the detailed morphological and structural analysis conducted in ASD and more recently in LMD, much work is still required to understand the complex mechanisms in SSID.

In this work, we introduced a new process, thin film solid state interfacial dealloying (thin-film-SSID), as a self-organizing method to form 3D interconnected bi-continuous metal-metal composites, which can be further treated to form high-surface porous metals at nano-/meso- scale thin films. Thin-film-SSID was demonstrated in Fe-Ni alloy films (50-50 at. %) using Mg films as the dealloying agent. Owing to the use of thin films as both precursor alloy and dealloying agent, the process can be applied to other substrates and a wider range of applications. The dealloying process was controlled under lower temperature and shorter time; this enables study of nano-size morphological evolution at the early stages of the dealloying process. Here we focus on studying the morphology of SSID at the interface between the dealloying front and the undealloyed region. The phase separation between Fe and Ni was characterized, with Fe ligaments being identified within the inter-diffusion layer. High resolution scanning transmission electron microscopy (STEM) revealed details of the elemental distribution, gap at the interface, and nano-size voids among the dealloyed ligaments. The phase separation and ligament shape were further analyzed in 3D by synchrotron X-ray fluorescence (XRF) nano-tomography and ptychography with hard X-ray nanoprobe. The X-ray absorption near edge structure (XANES) spectroscopy was used to confirm the composition of ligaments after dealloying. The influence of the surface dewetting, volume change, inter-diffusion, and other factors in thin film processing have also been discussed.

Results and Discussion

Phase separation and inter-diffusion in SSID

The schematic of thin-film-SSID sample preparation is shown in Figure S1 with details in the method section. A bi-layered structure of pristine sample is deposited on Si substrate: the bottom layer is a Fe-Ni precursor film, and the top layer is a Mg film. The analysis of an as-deposited sample (S100-P1) prior to dealloying is shown in Figure S2, including top-view and cross-section scanning electron microscope (SEM) images and cross-section energy-dispersive X-ray spectroscopy (EDX). No obvious feature or phase separation can be found in the pristine sample. After dealloying at the elevated temperature, the phase separation of Fe-Ni into Fe and Ni-Mg phases, introduced by Mg dealloying agent, can be clearly detected as discussed below; further detailed consideration of alternative hypotheses and the consideration of the corresponding different elemental and chemical signatures can be found in the Supporting Information.

The STEM analysis results of a dealloyed Fe-Ni film (S100-D1, 460˚C, 30 min) are shown in Fig. 1. Within the dealloyed region, several observations can be made: First, the Fe and Ni elemental distributions indicate that two phases, one Fe-rich and one Ni-rich, separate because of dealloying. Second, formation of ligaments of the Fe phase can be clearly identified within the dealloyed region. Third, in addition to the Fe and Ni elements, Mg is present in the dealloyed region and co-localizes with the Ni-rich phase. The quantitative analysis on the elemental distribution via line-profiling and co-localization of different elements are shown in Figure S4 and Figure S5, respectively, both further support the qualitative observation. These observations strongly suggest that the Mg dealloyed the Ni from initial Fe-Ni film, leading to the formation of Fe-rich and Ni_xMg phases. The resulting size of the Fe ligaments is less than 60 nm in diameter, which is much smaller than size fabricated by LMD methods[22]. Limited by the field of view and the 2D imaging, the formation of bi-continuous Fe and Ni_xMg in the dealloyed region will be further confirmed with 3D analysis shown in the later section.

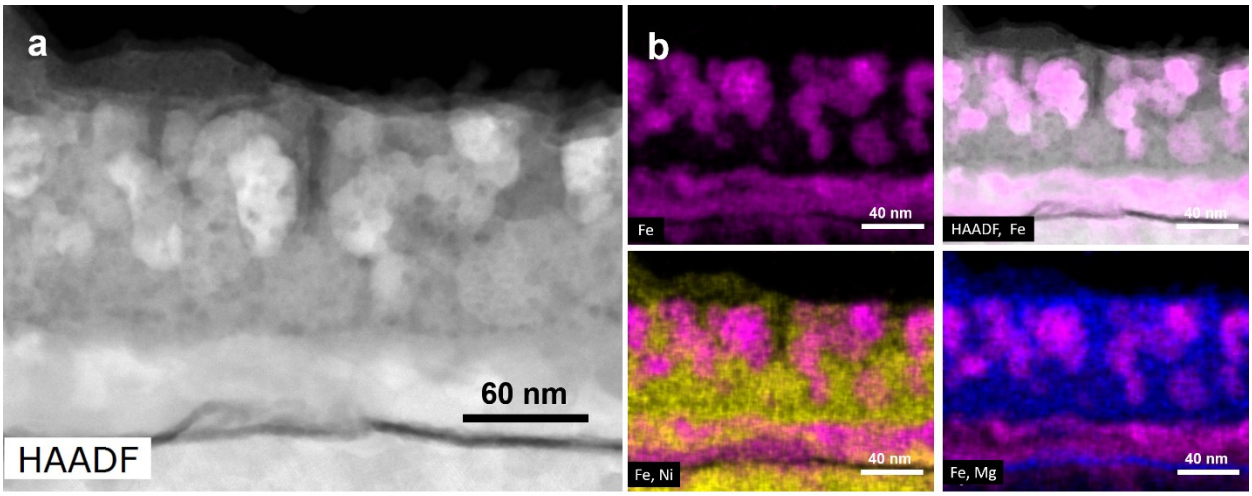

Fig. 1 STEM analysis of Fe-Ni films dealloyed by Mg film at 460˚C for 30 min (S100-D1) showing the morphology and composition at the dealloying front, indicating formation of Fe and Ni_xMg phases from dealloying. **a** High-angle annular dark-field image (HAADF) by -STEM, **b** EDX Analysis of Fe, HAADF-STEM with Fe, Fe and Ni, Fe and Mg.

Below the dealloyed region in Fe EDX map, a gap can be found at the interface between the dealloying front and undealloyed Fe-Ni region. The gap at the dealloying interface was previously characterized in the LMD[22]. This may be explained by Rayleigh instability, which is driven by

surface tension; the instability may break the cylindrical structures and form the gap at the interface. As a bi-continuous structure was formed instead of a bubble-like structure, such breakage is expected to only occur after the dealloying process.

Small nano-sized voids were found in the ligaments as shown in the HAADF image (Fig. 1.a). Similar voids have also been characterized in experiments and simulations in LMD and ASD processes[8-10]. There are different explanations for these voids: (1) Different ligaments collapsed and enclosed these voids. This movement is also related with imperfections within the structure and plasticity at ligaments' nodes[9]. (2) The voids formed during surface diffusion-controlled coarsening. The coarsening is related to the surface curvature and topological genus. It tends to reduce surface area, increases ligament width and reduces the genus. During coarsening, Rayleigh instabilities leads to bubble formation and ligament pinch-off. Different from ligament, bubble will separate from mass transport path. With longer time, separated bubbles will distribute much more randomly than ligaments, and will encapsulate into the metal ligament. (3) Voids are created by accumulation of lattice vacancies, which is supported by bulk diffusion and driven by concentration gradient. The mechanism of bulk diffusion was previously challenged by low diffusion rate in the room temperature for electrochemistry dealloying. However, it is possible in our SSID under relatively high temperature. However, from 2D STEM image, it is not clear if the voids are inside of the ligaments or among the surface of ligaments. Furthermore, the composition of the enclosed materials within the voids are also unclear. Collapsing ligaments and Rayleigh instability will result in enclosed materials within the void-like structure, whereas the vacancy diffusion will lead to empty voids. Further analysis, such as high-resolution STEM tomography is required to confirm the formation mechanisms of the void-like structures in SSID.

3D elemental distribution

The 3D XRF nano-tomography of a dealloyed sample (S100-D2) shown in Fig. 2 further confirms the phase separation of Fe and Ni-rich phases via thin-film-SSID. Fig. 2a shows 3D spatial distribution of Fe and Ni, and an overlapped view respectively. A layer with relatively homogenous Fe ligaments can be found. The ligaments with highly concentrated Fe can be clearly separated from Ni. The Ni layer is thicker than the Fe layer, and its surface is rough. Ni agglomeration can be found from the surface of film. The island-like/hillock Ni structure on top

of the Fe layer, is due to inter-diffusion of Mg and Ni. Further detailed analysis by TEM will be discussed in later sections.

Two sub-volumes were compared: one without the Ni_xMg agglomeration and one with the agglomeration on top of the bi-continuous features, as shown in Fig. 2b and c respectively. In Fig. 2b, the region without Mg_xNi agglomeration shows that at the interface between Fe and Ni phases, the concave Ni interface matches with the convex shape of Fe ligaments, which confirmed the spatial elemental separation in 3D. It is interesting that spatial elemental separation did not fully finish, and spatial overlap of Fe and Ni can be found in some limited regions, especially near the bottom of Fe layer. This may be explained as insufficient dealloying time or driving force for a complete dealloying; it is also possible that this is due to the spatial resolution limited by the instrument, which was unable to clearly separate the dealloyed region from the undealloyed region at the bottom, which would contain the Fe-Ni phase as expected. Nevertheless, the different spatial distribution of Fe-rich and Ni-rich structures in 3D XRF nano-tomography and their complementary shapes confirm the phase separation and Fe ligament formation. Besides, as shown in Fig. 2c, the Fe structure cropped from the region with Ni_xMg agglomeration shows a similar bi-continuous shape and size of Fe ligament to the Fe structure cropped from the region without the agglomeration.

Qualitatively, the Ni-rich phase has a much thicker ligament-like structure than the Fe phase; however overall the Fe and Ni-rich phases form a bi-continuous structure, confirming the observation from the 2D STEM. Such elemental separation is driven by mixing enthalpy difference between each element, mixing enthalpy of Fe-Ni and Mg-Ni are negative, with -2 KJ/mol and -4 KJ/mol respective, while the mixing enthalpy of Fe-Mg is positive with 18 KJ/mol[29]. The elements with negative mixing enthalpy would favor mixing, while elements with positive enthalpy would favor separation. Therefore, thermodynamically the Ni was expected to be dealloyed from Fe-Ni alloy by the Mg phase; however it was unclear prior to our experiment whether the bi-continuous structure may be achieved in thin films, where effects such as dimensional constraint, internal stress can play a role. Our experiment and 3D characterization demonstrated that despite of the compound phenomena, thin film processing can be effectively integrated with the SSID to design and create nano-/meso-scale metallic structures.

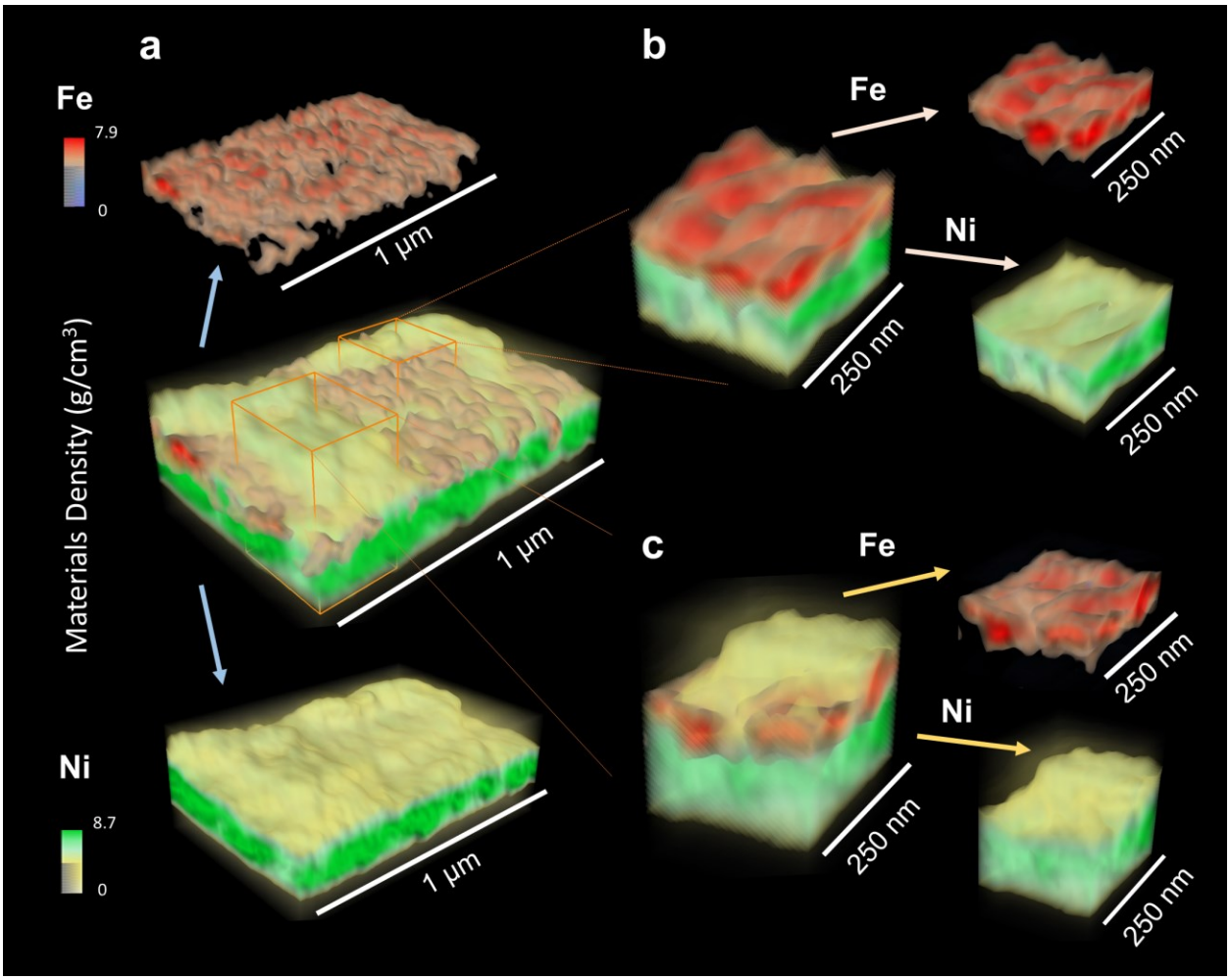

Fig. 2 3D XRF nano-tomography of Fe-Ni thin film dealloyed with Mg (S100-D2) by SSID at 460°C for 30 min from Hard X-Ray Nanoprobe (HXN) beamline at NSLS-II. **a** Representative volume shows Fe and Ni spatial distributions **b-c** Cropped sub-volumes to compare structures: **b** from the region without Ni agglomeration **c** from the region with Ni film agglomeration. Supplementary Video 1 based on the 3D XRF nano-tomography can be found in supporting information online. Color scale corresponds to the materials density (g/cm^3)

Previously in the LMD[23] and bulk SSID studies[26], a lamellar structure was observed with elongated ligaments along to the dealloying direction. However, no clear lamellar structure was observed here from the 3D XRF nano-tomography. It is possible that this is due to a dimensional effect in film structures. In addition, previously McCue *et al.* explained the mechanism of reorganizing surface of remaining structure after dealloying in LMD, including diffusion kinetics and curvature driven capillary forces[24]; the morphological evolution after dealloying in SSID may also experience similar process where the existing lamellar structure coarsened.

Dewetting in thin film and structural integrity

As also shown in the Fig. 2, after dealloying, the top surface of the film sample (S100-D4) shows an island-like/hillock feature in SEM images as shown in Fig. 3a. The width of the feature is in the range of 500 nm to 1 μm. The island-like/hillock features from the top-view SEM images are consistent with the Mg and Ni elemental distribution in the SEM EDX, also shown in Fig. 3a. This indicates that the island-like features are composed of Mg and Ni.

The composition of this interconnected island-like/hillock structure is further analyzed in a cross-sectioned thin lamella sample (S100-D1) by EDX in STEM, as shown in the Fig. 3. The size of the interconnected island-like/hillock structure seen in the STEM image is consistent with the island-like/hillock feature size on the top surface. The EDX mapping in STEM also shows that the composition of the island-like structure is Mg and Ni, indicating an inter-diffusion between the Ni and Mg during the dealloying process, where the Ni diffuses from Fe-Ni into the top Mg layer. SEM/STEM results are consistent with the 3D XRF nano-tomography (Fig. 2), where the distribution of Ni on the top layer corresponds to the island-like structure here. An oxidation layer was found on the top surface of the sample, which covers both the voids and the island-like/hillock structure; a MgO layer is likely present prior to dealloying when the surface of the Mg film is exposed to the air.

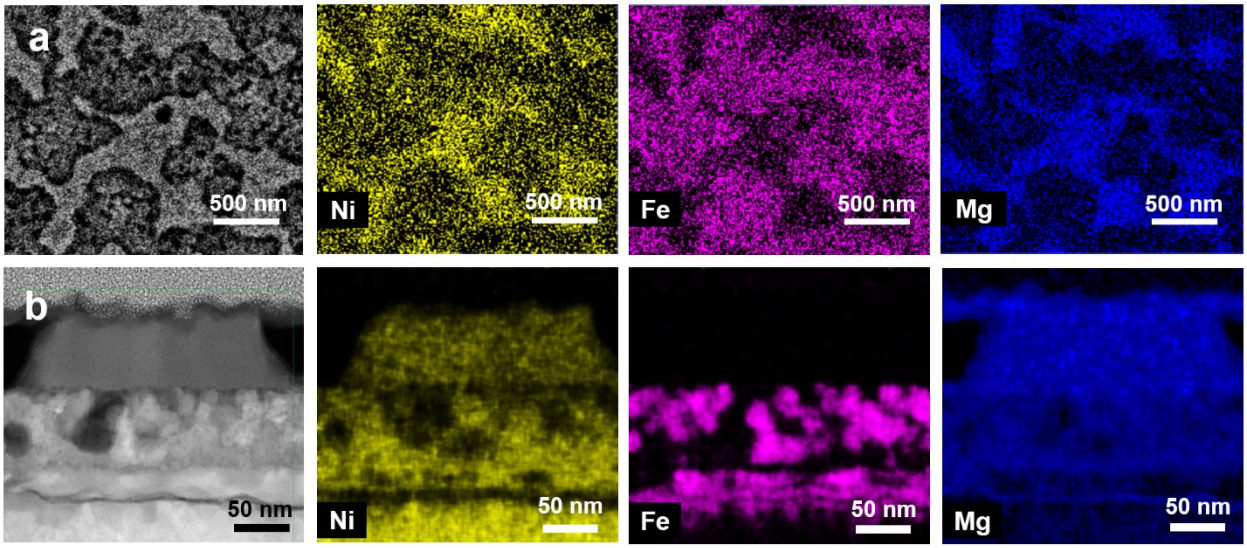

Fig. 3 a SEM and EDX analysis of Fe-Ni dealloyed with Mg (S100-D4) at 460°C for 30 min. SEM images show the island-like/hillock structure after dealloying: top view SEM with corresponding EDX analysis: Ni, Fe and Mg. **b** STEM analysis showing the morphology and composition at the dealloying front (S100-D1), indicating formation of Fe and Ni_xMg phases from dealloying: HAADF-STEM, and EDX map of the Ni, Fe and Mg elements Note that a Pt protection layer was deposited following a standard procedure for focus ion beam -scanning electron microscopy (FIB-SEM) cross-sectioning.

This continuous island-like structure may be attributed to a dewetting or agglomeration process in thin film processing. Similar structure has been widely characterized and analyzed[30-32]. Its driving force is to reduce the total energy of system, which can happen well below film's melting temperature. This process is generally started with void generation in the films, then followed by growth and segregation into islands. The void generation is believed to be driven by a stress relief process and followed by grooving from film surfaces, and then growth by surface diffusion of films[30, 32]. The rate of void growth can be accelerated by thickness of sample; the thinner of the films, the faster of the growth rate. In comparison, the dewetting process can hardly be found from a thicker sample (S300-D) prepared under the same dealloying condition, as shown in Figure S6. The dewetting process can also be influenced by wetting angle, voids growth by capillary pressure when reaching the critical radius. Besides, thin film deposition process, type of materials, and heat-treatment time, temperature and rate, will also influence agglomeration process, and even lead to thin film delamination[31-33]. This significant morphological change should be considered when preparing for bi-continuous thin films via SSID.

Previously, McCue *et al* prepared different diffusion couples for testing dealloying criteria in the solid metal dealloying process[28]. Their TiTa/Cu film sample experienced significant delamination after long time dealloying at higher temperature. They attributed the film failure to the volume changes from the formation of intermetallic, where the alloying/dealloying pairs deviates significantly from the Vegard's law[34, 35]. They further examined other systems which obey Vegard's law more closely (< 3% deviation), and no delamination was found. In our system, the parent alloy Fe-Ni also only has small deviation of 2.8% from Vegard's law. As such, even though the Mg and Ni will also form inter-metallic after dealloying, no delamination occurred in our system, which is consistent with the observation made by McCue *et al*. It is interesting to note that,

some other observations which differ from this assessment can be found in the literature. In Ti-Cu-Mg solid metal dealloying system, even more than 20% of deviation from Vegard's law in Cu-Mg did not limit the application of SSID process[27]. The Cu-Mg will also form inter-metallic structure after dealloying. Therefore, more complex mechanisms may play a role in determining the structural integrity of thin films in SSID processes; addressing the processing and structural parameters unique to thin films would be beneficial in future studies.

Inter-diffusion with the substrate and Kirkendall effect

As shown in the EDX maps near the bottom of the field of view (S100-D1), Ni was found to diffuse into the Si substrate. The diffusivity of Ni in Si is 3 to 4 orders of magnitude higher than Fe in Si[36, 37]. As a quick diffuser, much Ni diffused into the Si substrate, while few Fe diffused into the Si substrate, as seen in EDX result shown in Fig. 3. As a result, Ni is present near the interface between films and substrate, where undealloyed Fe is present. The gap in the Ni EDX mapping corresponds to the interface between deposited thin film and Si substrate. It is possible that this Ni diffusion into the Si limited further dealloying of Fe-Ni by Mg. Insufficient Ni remained in the undealloyed Fe-Ni region, limiting the dealloying process and movement of dealloying front stopped.

Previously, Ni inter-diffusion with Si wafer has also been well characterized and analyzed. Ni-Si inter-diffusion and compound formation have been reported that the NiSi will form between Ni-Si thin film with around 400°C heat treatment[38]. Thron *et al.* found that Ni will inter-diffuse into Si substrate once being deposited[39]. From TEM cross section, they identified a multi-layer structure including amorphous SiO_2, polycrystalline Ni, crystal Ni_2Si and $NiSi_x$ solid solution. To examine the nature of the Ni and Si substrate inter-diffusion, we analyzed the cross-section of the as-deposited pristine sample (S100-P1) by TEM, shown in Figure S8. We found a low-density layer with thickness of ~2.5 nm between the deposited films and Si substrate. While the precise composition of this thin layer cannot be identified, this layer may be a native SiO_2 layer. While Mayer *et al.* showed that the native SiO_2 on the Si wafer can delay and even act as barrier layer between Ni thin films and Si wafer[40], it is likely that both high concentration of defects among native SiO_2 layer and intrinsic stress during film deposition contribute to the diffusion of Ni through SiO_2 to Si substrate[39]. Further analysis on thin film processing and substrate effects needs

to be carefully considered, including understanding the dimensional effect, size-effect at nano-meter length scale, stress and strain distribution within thin films, and substrate effect for the SSID materials design.

This inter-diffusion between Ni and Si also likely lead to Kirkendall effect, forming voids within the films. Large micron-sized voids were found within the dealloyed layer from cross-section STEM (S100-D1) (Fig. 3) and reconstruction ptychography 2D projection image (S100-D2) (Figure S10). This can be explained by Kirkendall effect, that the Ni diffusivity is much higher than other element in this system, leaving voids and space in materials with higher diffusivity. Previous experimental results showed that no voids were detected in the inter-diffusion layer between Mg and Ni[41]; the diffusivity difference between Ni and Mg was believed only in the ratio of 1.5[42]. Therefore, it is hard to generate such voids from inter-diffusion between Mg and Ni. Instead, it is more likely that the high diffusivity of Ni in the Si substrate leads to the generation of voids by Kirkendall effect[36].

To test this hypothesis of Kirkendall effect, a testing Mg-Ni bi-layer film (S100-K) was deposited on the Si substrate and was heated at 460˚C for 30 min. Result is shown in Figure S9. The voids can also be found within the inter-diffusion layer and distribute closer to the interface between the Ni film and the Si substrate. Therefore, it is confirmed that the voids within the dealloyed layer is due to Kirkendall effect between the Ni film and Si substrate. Similar voids can also be found in the thicker samples (S300-D), near the boundary between dealloyed Fe-Ni layer and Si substrate, as shown in Figure S6.

From this observation, while the bi-continuous structure formation was successful, despite the presence of the Ni diffusion into the substrate, future work may be conducted to control such film-substrate inter-diffusion; the phenomena may be mitigated by introducing a diffusion barrier layer between the dealloying films and the substrate such as Al_2O_3[43].

Structure and chemical composition analysis of bi-continuous films

To fully resolve the structure and chemical composition of the dealloyed bi-continuous structure, analysis conducted by TEM diffraction on the cross-section sample (S100-D1) and synchrotron X-ray absorption spectroscopy on a film sample (S100-D3) are shown in Fig. 4.

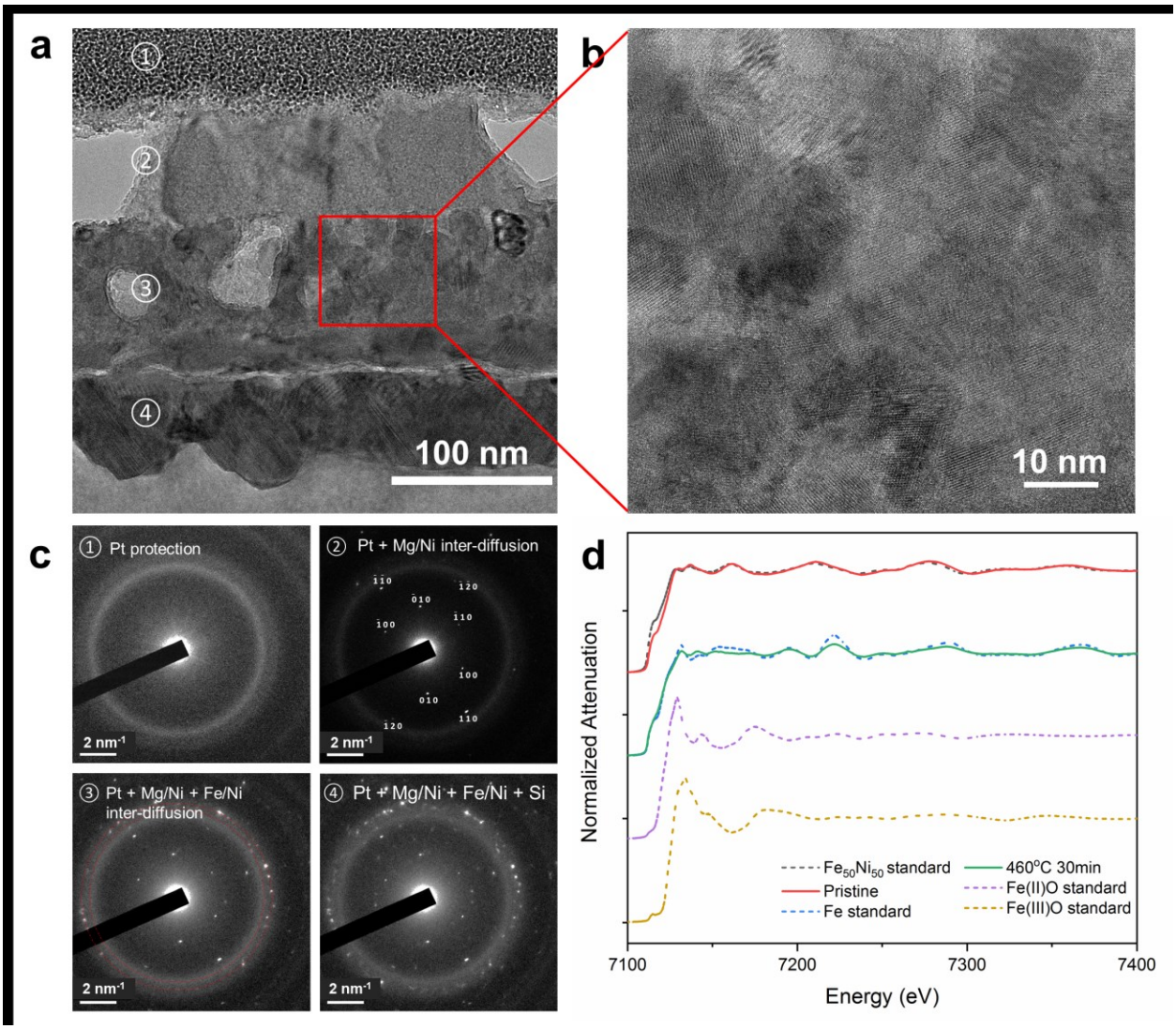

Fig. 4 a TEM image of Fe-Ni films dealloyed with Mg under 460°C for 30 min (S100-D1). **b** Zoom-in view of TEM image on separate Fe and Ni-Mg inter-diffusion layer **c** The SAEDs were collected from the top to the bottom, including, including Pt protection layer, Pt with Mg–Ni interdiffusion layer, Pt with Mg–Ni and Fe–Ni interdiffusion layers, and all film layers with a Si substrate. **d** XANES was collected on Fe, Fe(II)O, Fe(III)O, FeNi (50-50 at.%) standard powder, pristine (S100-P2) and sample dealloyed at 460°C for 30 min (S100-D3).

From Fig. 4a and Fig. 4b, polycrystalline Ni_xMg agglomeration region, Fe/Ni-Mg inter-diffusion layer, and the Ni-Si inter-diffusion layer can be clearly identified. The SAED with TEM images were collected from the pristine sample (S100-P1) as shown in Figure S8 and the one after

dealloying at 460˚C for 30 min (S100-D1), shown in Fig. 4c. Crystal structure of pristine Mg layer can be identified from SAED. The crystalline information of the pristine Fe-Ni layer from SAED however is not clear, potentially due to the overlapping of the peaks and instrumentation limitation of the aperture size. The TEM image reveals a column-like and granular structure, suggesting that the pristine sample to be polycrystalline. Further systematic studies on the evolution of crystalline structure in thin film SSID may be conducted.

As indicated from the SAED analysis, the composition of the hillock structure is Ni_2Mg. This is consistent with the Mg-Ni phase diagram and prior study that Mg_2Ni and Ni_2Mg are present as intermetallic[44]. The SAED on Fe-Ni inter-diffusion dealloyed layer is not clear. Only two emerging rings appeared; the inner diffraction ring may be attributed to FeO (2 0 0), and the outer ring may be attributed to Fe (1 0 0), $FeNi_3$ (1 1 1), Fe_2O_3 (0 2 4) and Ni (1 1 1). Further analysis on the Fe-rich phase was resolved by XANES, discussed in the later section.

The polycrystalline structure has a direct impact on the diffusion distance during the dealloying process. According to density functional theory (DFT) based simulation results, under the same heating time and temperature, the distance of dilute Ni diffuse in Mg[45, 46] (including both parallel and perpendicular to the c-axis in the Mg) can be several times longer than the thickness of our S100 samples. On the other hand, previous experimental result[47] indicates that diffusion rate can be even faster than the simulation result, which was explained as their result was collected from samples with smaller grain structure; diffusion through grain boundary is faster than the dilute diffusion in the simulation. In our experiment, after dealloying process, polycrystalline structure with different crystal orientations can clearly be found from the Fe/Ni-Mg inter-diffusion layer, as shown in Fig. 4b. The diffusion through small grains can also lead to faster diffusion than the dilute diffusion in the simulation result. According to the simulation result, diffusion distance of Ni in Mg under 430˚C for 7.5 min can reach 300.78 nm, and diffusion of Mg in Ni is only 0.05 nm[45, 46]. While estimated diffusion distance of Mg in Ni based on the previous experimental result was 492.43nm, calculated from the provided diffusion coefficient and activation energy[47]. As shown by EDX in Figure S7 of a thicker sample (S300-D-L) dealloyed under 430˚C for 7.5 min, Mg and Ni have fully inter-diffused into each other. Diffusion distance in our experiment is faster than predicted from the simulation result and is more consistent with the previous experimental results based on polycrystalline structure.

The XANES analysis showed oxidation state and chemical composition of the dealloyed sample (S100-D3). Fe K-edge XANES spectra are shown in Fig. 4d, and Ni K-edge XANES spectra are shown in Figure S11. The Fe K-edge position in XANES spectrum from pristine sample (S100-P2) is very close to the standard of Fe-Ni powders (50-50 at. %), and their slight difference can be attributed to a slight compositional variation and a strain distribution within the metallic thin film. Moreover, the similarity at the beginning of extended X-ray absorption fine structure (EXAFS) oscillation indicates that the local configuration of the pristine film is close to the powder standards. After dealloying, the Fe K-edge XANES of dealloyed sample shows a metallic Fe structure, confirming the formation of Fe ligaments from dealloying. Furthermore, compared with the standard Fe foil, the spectrum showed a 'dampened' XANES region and a less affected EXAFS region; this suggests that the Fe structure after dealloying forms nano-sized small domains in the sample, therefore suppressing of multi-scattering events in the XANES region. The formation of nano-sized domains is also consistent with the TEM result as shown in Fig. 4b. Little difference was found between the Ni K-edge spectra of the pure Ni and Fe-Ni powders (50-50 at.%); it is expected from the literature that the Fe K-edge XANES spectra will show more significant difference than the Ni K-edge spectra between metal and intermetallic materials, both exhibit zero oxidation states[49]. Notable changes occurred in the Ni K-edge XANES of dealloyed sample (S100-D3), which was not identified as either the Ni(0) phases (pure Ni or Ni intermetallic) or nickel oxides; based on the SAED result, it is expected to form Ni_2Mg.

Summary of morphological evolution and structural formation in SSID thin films

A summary of the overall morphological evolution and structural formation of thin-film-SSID can be found in Fig. 5 and Supplementary Video 1. A polycrystalline Fe-Ni (50-50 at. %) film was deposited onto Si substrate, followed by a polycrystalline Mg film deposited on the top, forming the pristine sample. After dealloying at 460˚C for 30 min, the micron size agglomeration of Ni_2Mg, resulted from thin film dewetting formed an island-like/hillock structure on the top layer. This structure did not influence formation of bi-continuous nanosized Fe/Ni-Mg ligaments underneath. In the inter-diffusion layer, Mg drives the dealloying of Fe-Ni, forming separate Fe and Ni_2Mg bi-continuous ligaments. The Fe phase formed nano-sized domains and contained even smaller voids. Large voids also distribute between separated Fe/Ni-Mg ligaments, which was caused by the Kirkendall effect between Ni and Si substrate interdiffusion, with Ni being the faster diffuser. At

the bottom, undealloyed Fe-Ni phase remains on the top of Si substrate, with some Ni and Mg diffuse into the Si substrate.

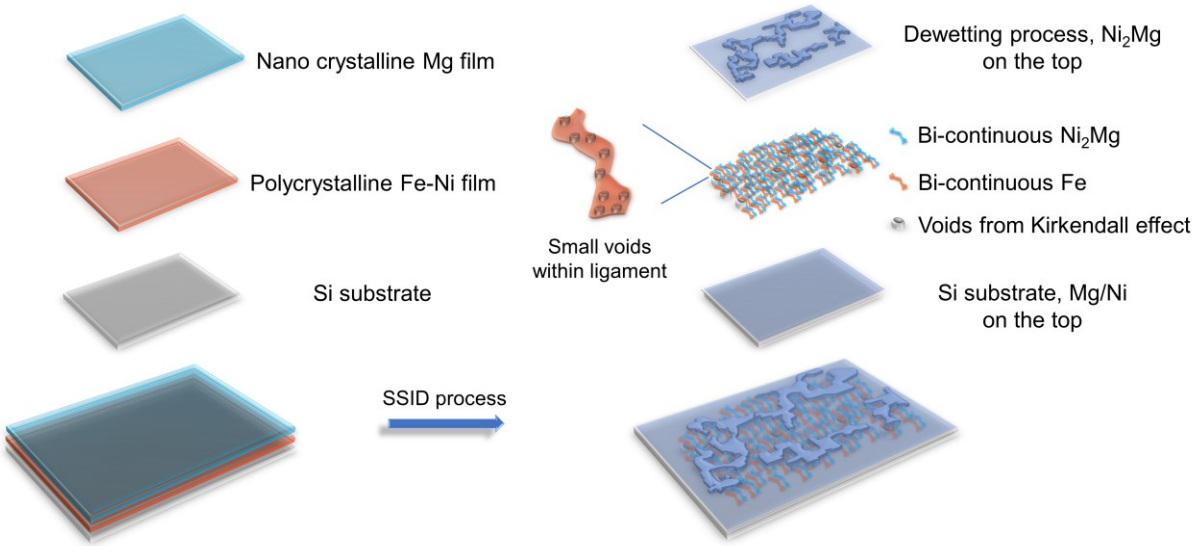

Fig. 5 Schematic of morphological evolution of thin-film-SSID in Fe-Ni/Mg system.

Conclusion

Thin-film-SSID as a new method to fabricate 3D bi-continuous structure was first demonstrated in Fe-Ni films (50-50 at. %), using Mg films as the dealloying agent. The self-organizing dealloying process, induced by mixing enthalpy difference leading to a formation of bi-continuous structure of Fe and Ni_2Mg was identified and characterized by by multimodal characterization – a combination of electron-based imaging and diffraction, as well as synchrotron X-ray nano-probe 3D XRF nano-tomography and absorption spectroscopy. The critical signatures of dealloying, Fe-Ni+ Mg → Mg-Ni + Fe, were observed and further quantified, including 1) co-localization of Mg and Ni in elemental distribution, and separation of Fe with Mg and Ni, as observed in STEM and XRF nano-tomography, and 2) chemically, a mixture of Fe-Fe and Fe-Ni bonds were converted into Fe-Fe bonds, namely that Fe atoms coordinate with other Fe atoms only, as observed in XANES.

Morphological and elemental distribution details were further characterized by a multi-scale imaging of X-ray and electron microscopy. STEM analysis showed a clear phase separation between the Fe ligaments and Ni-rich (Ni-Mg) phase in qualitative visualization as well as quantitative line-profiles and cross-correlations; the composition from each phase was further confirmed and directly visualized in 3D by the advanced synchrotron X-ray fluorescence nano-tomography and ptychography. Small voids among the ligaments were identified in the SSID system. A gap between the dealloying front and the undealloyed region were identified and potential mechanisms were discussed.

The crystal structure and oxidation evolution in the SSID have also been characterized. The starting Fe-Ni pristine film was believed to be polycrystalline and further systematic studies on the effects of the crystallinity of the pristine films and structural evolution of SSID thin film would be beneficial. The dealloyed structure showed polycrystallinity in the STEM images. The formation of pure Fe ligament after dealloying has been confirmed by XANES, which further suggested that the Fe phase formed nano-crystalline domains.

Additional phenomena in the thin film processing-structure relationship have also been discovered and analyzed. An agglomeration/dewetting process was found to form island-like/hillock structures on the surface of films, especially when the film thickness is thin. Inter-diffusion of Ni with Si substrate led to voids formation and Kirkendall effects. While these processes did not hinder the formation of the bi-continuous structure, future processing and materials design shall consider the effects of these phenomena. To alleviate the side effects induced by thin film process, controlling film thickness, pristine film composition, deposition process and selecting barrier layers to minimize the inter-diffusion are crucial. By demonstrating the new concept of thin film-SSID, this work sets directions for future work in both fundamental studies for mechanistic understanding, processing innovation and developing applications. We propose that in the future, high-resolution 3D characterization as well as systematic studies of materials and processing parameters, in conduction with theoretical modeling, need to be conducted to further understand the kinetics mechanisms in thin-film-SSID. Applying thin-film-SSID to other material systems, as well as driving new functional application, are new opportunities in materials design.

Methods

Sample preparation

The schematic of thin-film-SSID preparation is shown in Figure S1. Sputtering targets (99.95% purity from Stanford Advanced Materials) with composition of Ni-Fe at 50-50 at. %, and Mg were used to prepare precursor and dealloying agent thin films respectively, via sputtering deposition. <100> silicon wafers (University Wafer) were cut to 1×1 cm^2 square size, as substrates for thin film deposition. The wafers were treated first by oxygen plasma for cleaning the wafer surface. The Fe-Ni and Mg thin films were sequentially sputtered onto the Si wafer substrates.

Two types of samples were prepared with different thickness for characterization: 1) S100 samples: Thinner film samples of ~ 100 nm for both precursor and dealloying agent layers with 95.08 ± 4.29 nm Fe-Ni films and 94.43 ± 6.78 nm Mg films were deposited, and 2) S300 samples: Thicker film samples of ~ 300 nm for both layers with 280.58 ± 8.63 nm Fe-Ni films and 354.68 ± 40.92 nm Mg films. The roughness of Mg film increases significantly when deposited as a thicker layer, while thicker thickness Fe-Ni films remain relative smooth. This leads to significant Mg layer thickness variation in S300 samples. In addition, to study Kirkendall effect, pure Ni layer was deposited to a Si wafer substrate followed by deposition of a Mg layer. The thickness, deposition process and heat treatment were similar to S100 samples, named as S100-K. A calibrated quartz oscillator crystal was used to monitor the film thickness during sputtering deposition. The silicon wafer substrate temperature was kept at 25˚C.

After deposition, samples were heated by Rapid Thermal Processing (Modular Process Technology Corp.) method for isothermal heat treatment to introduce dealloying. All the heat treatment processes were conducted in a reduced atmosphere (4% hydrogen and 96% Argon) to prevent oxidation during the heat treatment. Samples were heated from room temperature to the designated dealloying temperature in 30 s and kept at the dealloying temperature for a designated duration; then cooled down to room temperature in ~150s. The heating temperature was set to be lower than the Mg melting temperature so the dealloying process was conducted in solid-state. The heating temperature and time for both types of samples were determined based on the estimated diffusion length calculated from the diffusion data in the literature[46, 50]. For S100 samples (thinner samples), the dealloying was conducted at 460˚C for 30 min, which was expected to be sufficient for dealloying via inter-diffusion between Fe-Ni and Mg layer to complete. One S100-K was

heated at 460˚C for 30 min for comparison. As a general information, the heat treatment and cooling were conducted via a rapid thermal process (RTP). The ramp up rate was 14.5 °C/s, and cooling rate was 3 °C/s as measured by the thermocouple connected to the substrate; and during the cooling Ar/H_2 (4 v/v%) was flushed through the system and thus the cooling rate at the surface of the thin film might be even faster. Here we do not consider the kinetics effect of the heating and cooling rate quantitatively, as those would require further careful analysis, which could be a topic of future studies. One S300 (S300-D) used the same dealloying temperature and time condition (460˚C, 30 min), an additional S300 sample (name as S300-D-L) was heated at 430˚C for 7.5 min; the lower dealloying temperature and shorter dealloying time in the thicker sample were used to create a partially dealloyed structure for observing the early-stage dealloying mechanism in this system. Base on the phase diagram, while dealloyed at the slightly lower temperature, the sample was expected to follow a consistent phase transformation process as in the 460˚C.

Multiple samples were prepared under the same conditions and used in different characterization techniques, as detailed below. A list of samples and corresponding techniques can be found in the Supporting Information.

Characterization

STEM with Energy-dispersive X-Ray spectroscopy (EDX), transmission electron microscopy (TEM) were conducted on S100-D1, and synchrotron X-ray nano-probe tomography (fluorescence and ptychography) were conducted on S100-D2, to study the morphology and elemental distribution with high resolution and at 3D, respectively. Synchrotron X-ray absorption spectroscopy was also conducted on S100-D3 to study the oxidation state of the dealloyed films. For samples, including S100-P1, S100-D4, S100-K, S300-P, S300-D and S300-D-L, SEM was used to study the surface morphology and focus ion beam -scanning electron microscopy (FIB-SEM) to study the cross-section morphology. EDX analysis was also carried out in the SEM to study elemental distribution. Samples with their corresponding characterization are listed in Table S1 of the supporting information. The details of each technique are described below:

FIB-SEM sample preparation

FIB-SEM (Helios dual beam) was used to prepare S100 samples, including S100-P1, S100-D1 and S100-D2 for STEM analysis and X-ray nano-probe tomography. STEM sample was prepared following standard sample preparation procedure to create a thin lamella with thickness less than 100 nm for electron transparency. The X-ray nano-probe tomography sample was milled to a cylindrical shape with a diameter of 1.5 μm and the length of 8 μm. In addition, FIB milling was also used to create cross-section samples from S100-P1, S100-D4, S100-K, S300-P, S300-D and S300-D-L, for SEM imaging and thin lamella samples for EDX mapping in SEM.

STEM, TEM, SEM and EDX analysis

STEM characterization was carried out in a TEM (Talos model from FEI), operating at 200 keV. High-angle annular dark-field imaging (HAADF) and EDX analysis were conducted to study the morphology and elemental distribution within the sample after SSID process. Selected area electron diffraction (SAED) was conducted using a different instrument, in a JEOL 1400 TEM, which operates at 120 keV. The SEM and EDX analysis were conducted in scanning electron microscope (SEM, JEOL 7600F); all EDX in SEM cross-section results shown were conducted on thin sectioned samples (~ 100 nm thick) prepared by FIB for better spatial resolutions. The SEM/EDX, FIB-SEM, STEM/EDX, and TEM/SAED analysis was conducted at the Center for Functional Nanomaterials (Brookhaven National laboratory).

Synchrotron X-ray nano-probe tomography

Synchrotron 3D XRF nano-tomography and ptychographic tomography was conducted at Hard X-ray Nanoprobe (HXN) beamline 3-ID at National Synchrotron Light Source II (NSLS-II) (Brookhaven National Laboratory). A Multilayer Laue Lens with optical resolution of 10 nm was used for focusing the X-ray beam onto the sample[51]. 2D XRF images were collected with a 2° angular step size, with a total of 126° angular range (63 XRF images) were collected. Scanning area of each frame is 3 × 2 μm^2 with 10 nm step size. Incident X-ray beam energy is 12 KeV, above Fe and Ni absorption K-edges. At each scanning point, a fluorescence spectrum was collected with a dwell time of 0.04s.

The transmitted scattering pattern was collected by a Merlin detector with 55 μm pixels placed 0.5 m downstream from the sample. This dataset was used for ptychography reconstruction to provide phase-contrast images with enhanced spatial resolution.

Synchrotron X-ray absorption spectroscopy

Synchrotron Fe K-edge and Ni K-edge XANES spectra of the as deposited S100-P2 and dealloyed S100-D3 were collected at Beamline for Materials Measurement (BMM), beamline 6-BM at NSLS-II (Brookhaven National Laboratory). XANES spectra were collected from both film samples on Si substrate in fluorescence mode; grazing incident geometry was used to maximize the footprint of the beam on the sample for optimal signal-to-noise ratio. To mitigate the influence of X-ray diffraction rising from crystalline Si substrate, samples were constantly rotated during data collection. The Fe and Ni foils, Fe(II)O (Sigma Aldrich), Fe(III)O (Sterm Chemicals, Inc.), $Fe_{50}Ni_{50}$ (Goodfellow) and Ni(II)O (Alfa Aesar) powder standards were measured in transmission mode. To improve signal-to-noise ratio, three scans were collected and averaged for each sample at each specific energy edge.

Data processing and analysis

The fluorescence spectra from all pixels in XRF mapping were fitted individually using PyXRF[52], a fluorescence analysis package developed at NSLS-II, to create XRF images for the present elements. To align the XRF images for XRF tomographic reconstruction, ImageJ[53] based plugin MultiStackRegistration[54] was applied. Alignment was firstly applied on Ni fluorescence frame, and then transformation matrix was applied to align other elements' fluorescence images. The XRF nano-tomography was reconstructed based on the fitted XRF images using Python based package TomoPy[55]. Tomographic reconstruction algorithm was selected as "ospml_quad", with 100 times of iterations. The volume rendering, and visualization were performed using software Avizo (9.0 FEI).

The ptychography reconstruction was conducted with 80 iterations of the difference map algorithm. This computation heavy process was accelerated with distributed GPU[56]. To accommodate blurry in scattering pattern introduced by the on-the-fly scan scheme, 4 illumination modes were included in the reconstruction process[57]. The scattering intensity extends to the edge of a 188x188 pixel area, which gives 5 nm reconstruction pixel size.

The XANES spectrum was analyzed by Athena package following standard background subtraction and normalization procedure[58]. Comparison between standard sample and thin film

samples for finger printing were also conducted. The data acquisition and management at NSLS-II were conducted via Bluesky and Data Broker packages.[59]

Reference

1. A. Wittstock, V. Zielasek, J. Biener, C. M. Friend and M. Baumer, *Science*, 2010, **327**, 319-322.
2. J. Snyder, T. Fujita, M. W. Chen and J. Erlebacher, *Nat. Mater.*, 2010, **9**, 904-907.
3. T. Wada, T. Ichitsubo, K. Yubuta, H. Segawa, H. Yoshida and H. Kato, *Nano Lett.*, 2014, **14**, 4505-4510.
4. C. H. Zhao, T. Wada, V. De Andrade, D. Gursoy, H. Kato and Y. C. K. Chen-Wiegart, *Nano Energy*, 2018, **52**, 381-390.
5. E. M. Bringa, J. D. Monk, A. Caro, A. Misra, L. Zepeda-Ruiz, M. Duchaineau, F. Abraham, M. Nastasi, S. T. Picraux, Y. Q. Wang and D. Farkas, *Nano Lett.*, 2012, **12**, 3351-3355.
6. J. Rugolo, J. Erlebacher and K. Sieradzki, *Nat. Mater.*, 2006, **5**, 946-949.
7. J. Erlebacher, M. J. Aziz, A. Karma, N. Dimitrov and K. Sieradzki, *Nature*, 2001, **410**, 450-453.
8. J. Erlebacher, *Phys. Rev. Lett.*, 2011, **106**, 225504-225501-225504.
9. K. Kolluri and M. J. Demkowicz, *Acta Mater.*, 2011, **59**, 7645-7653.
10. H. Rosner, S. Parida, D. Kramer, C. A. Volkert and J. Weissmuller, *Adv. Eng. Mater.*, 2007, **9**, 535-541.
11. S. Parida, D. Kramer, C. A. Volkert, H. Rosner, J. Erlebacher and J. Weissmuller, *Phys. Rev. Lett.*, 2006, **97**.
12. Y. C. K. Chen, Y. S. Chu, J. Yi, I. McNulty, Q. Shen, P. W. Voorhees and D. C. Dunand, *Appl. Phys. Lett.*, 2010, **96**, 043122-043121-043123.
13. Y. C. K. Chen-Wiegart, S. Wang, W. K. Lee, I. McNulty, P. W. Voorhees and D. C. Dunand, *Acta Mater.*, 2013, **61**, 1118-1125.
14. Y. C. K. Chen-Wiegart, S. Wang, Y. S. Chu, W. J. Liu, I. McNulty, P. W. Voorhees and D. C. Dunand, *Acta Mater.*, 2012, **60**, 4972-4981.
15. Y. C. K. Chen-Wiegart, S. Wang, I. McNulty and D. C. Dunand, *Acta Mater.*, 2013, **61**, 5561-5570.
16. B. Pfeiffer, T. Erichsen, E. Epler, C. A. Volkert, P. Trompenaars and C. Nowak, *Microsc. Microanal.*, 2015, **21**, 557-563.
17. N. Badwe, X. Chen, D. K. Schreiber, M. J. Olszta, N. R. Overman, E. K. Karasz, A. Y. Tse, S. M. Bruemmer and K. Sieradzki, *Nat. Mater.*, 2018, **17**, 887-+.
18. T. Wada, Kato, H., *Scr. Mater.*, 2013, **68**, 723-726.
19. M. Tsuda, T. Wada and H. Kato, *J. Appl. Phys.*, 2013, **114**, 113503-113501-113508.
20. S. G. Yu, K. Yubuta, T. Wada and H. Kato, *Carbon*, 2016, **96**, 403-410.
21. Y. C. K. Chen-Wiegart, T. Wada, N. Butakov, X. H. Xiao, F. De Carlo, H. Kato, J. Wang, D. C. Dunand and E. Maire, *J. Mater. Res.*, 2013, **28**, 2444-2452.
22. C. Zhao, T. Wada, V. De Andrade, G. J. Williams, J. Gelb, L. Li, J. Thieme, H. Kato and Y.-C. K. Chen-Wiegart, *ACS Appl. Mater. Interfaces*, 2017, **9**, 34172-34184.
23. P. A. Geslin, I. McCue, B. Gaskey, J. Erlebacher and A. Karma, *Nat. Commun.*, 2015, **6**, 8887-8881-8888.
24. I. McCue, A. Karma and J. Erlebacher, *Mrs Bulletin*, 2018, **43**, 27-34.
25. I. McCue, B. Gaskey, P. A. Geslin, A. Karma and J. Erlebacher, *Acta Mater.*, 2016, **115**, 10-23.
26. T. Wada, K. Yubuta and H. Kato, *Scr. Mater.*, 2016, **118**, 33-36.

27. F. M. Zhang, P. Li, J. Yu, L. L. Wang, F. Saba, G. Dai and S. Y. He, *J. Mater. Res.*, 2017, **32**, 1528-1540.
28. I. McCue and M. J. Demkowicz, *Jom*, 2017, **69**, 2199-2205.
29. A. Takeuchi and A. Inoue, *Mater. Trans.*, 2005, **46**, 2817-2829.
30. C. V. Thompson, *Annu. Rev. Mater. Sci.*, 2012, **42**, 399-434.
31. S. L. Firebaugh, K. F. Jensen and M. A. Schmidt, *J. Microelectromech. Syst.*, 1998, **7**, 128-135.
32. J. Y. Kwon, T. S. Yoon, K. B. Kim and S. H. Min, *J. Appl. Phys.*, 2003, **93**, 3270-3278.
33. R. M. Tiggelaar, R. G. R. Sanders, A. W. Groenland and J. G. E. Gardeniers, *Sens. Actuators, A*, 2009, **152**, 39-47.
34. H. W. King, *J. Mater. Sci.*, 1966, **1**, 79-90.
35. A. R. Denton and N. W. Ashcroft, *Phys. Rev. A*, 1991, **43**, 3161-3164.
36. J. Lindroos, D. P. Fenning, D. J. Backlund, E. Verlage, A. Gorgulla, S. K. Estreicher, H. Savin and T. Buonassisi, *J. Appl. Phys.*, 2013, **113**.
37. E. R. Weber, *Appl. Phys. A - Mater*, 1983, **30**, 1-22.
38. K. N. Tu, G. Ottaviani, U. Gosele and H. Foll, *J. Appl. Phys.*, 1983, **54**, 758-763.
39. A. M. Thron, P. K. Greene, K. Liu and K. van Benthem, *Acta Mater.*, 2012, **60**, 2668-2678.
40. J. T. Mayer, R. F. Lin and E. Garfunkel, *Surf. Sci.*, 1991, **265**, 102-110.
41. M. Y. Tsai, M. H. Chou and C. R. Kao, *J. Alloys Compd.*, 2009, **471**, 90-92.
42. Q. Z. Hong and F. M. Dheurle, *J. Appl. Phys.*, 1992, **72**, 4036-4040.
43. E. Ozceri and Y. Selamet, *J. Phys. D. Appl. Phys*, 2015, **48**.
44. P. S. Wang, J. R. Zhao, Y. Du, H. H. Xu, T. Gang, J. C. Fen, L. J. Zhang, C. Y. He, S. H. Liu and H. W. Ouyang, *Int. J. Mater. Res.*, 2011, **102**, 6-16.
45. B. C. Zhou, S. L. Shang, Y. Wang and Z. K. Liu, *Acta Mater.*, 2016, **103**, 573-586.
46. H. Wu, T. Mayeshiba and D. Morgan, *Sci. Data*, 2016, **3**.
47. H. W. Allison and H. Samelson, *J. Appl. Phys.*, 1959, **30**, 1419-1424.
48. T. Wada, K. Yubuta, A. Inoue and H. Kato, *Mater. Lett.*, 2011, **65**, 1076-1078.
49. Q. Bi, X. Wang, F. Gu, X. Du, H. Bao, G. Yin, J. Liu and F. Huang, *Chemsuschem*, 2017, **10**, 3044-3048.
50. B. C. Zhou, S. L. Shang, Y. Wang and Z. K. Liu, *Data in Brief*, 2015, **5**, 900-912.
51. E. Nazaretski, H. Yan, K. Lauer, X. Huang, W. Xu, S. Kalbfleisch, L. Li, N. Bouet, J. Zhou, D. Shu, R. Conley and Y. S. Chu, Brookhaven Natl Lab, NY, 2015.
52. L. Li, *Journal*, 2015, Fluorescence fitting GUI.
53. C. A. Schneider, W. S. Rasband and K. W. Eliceiri, *Nat. Methods*, 2012, **9**, 671-675.
54. P. Thevenaz, U. E. Ruttimann and M. Unser, *IEEE Trans. Image. Process*, 1998, **7**, 27-41.
55. D. Gürsoy, F. De Carlo, X. Xiao and C. Jacobsen, *J. Synchrotron Radiat.*, 2014, **21**, 1188-1193.
56. D. Zhihua, Y. L. L. Fang, H. Xiaojing, Y. Hanfei, H. Sungsoo, X. Wei, Y. S. Chu, S. I. Campbell and L. Meifeng, *2018 New York Scientific Data Summit (NYSDS). Proceedings*, 2018, DOI: 10.1109/nysds.2018.8538964, 5 pp.-5 pp.
57. X. J. Huang, K. Lauer, J. N. Clark, W. H. Xu, E. Nazaretski, R. Harder, I. K. Robinson and Y. S. Chu, *Sci. Rep.*, 2015, **5**.
58. B. Ravel and M. Newville, *J. Synchrotron Radiat.*, 2005, **12**, 537-541.
59. http://blueskyproject.io

Acknowledgements

Y.-c. K. C.-W, Mingzhao L. and C.Z. developed the research idea. Y.-c. K. C.-W. and C. Z. wrote user proposals for the use of BMM and HXN beamlines at NSLS-II and equipment at CFN. C. Z. conducted thin film deposition under the training and direction of Ming L. and Mingzhao L.; C.-H. L. gave valuable advice on the thin film deposition process. C. Z. conducted an RTP heating process under the training and direction of Mingzhao L.; K. K. conducted a TEM sample preparation by FIB-SEM; K. K. conducted EDX/STEM analysis, with the participation of C. Z. and Y.-c. K. C.-W. C. Z. conducted FIB-SEM for additional sample preparations for SEM/EDX and further TEM analysis. F. C. and C. Z. conducted TEM with SAED characterization; C. Z. conducted SEM analysis initially under the training and assistance of F. C., and conducted further analysis individually. X. H., H. Y. E. N. and Y. C. designed and commissioned the HXN beamline. C. Z., X. H., H. Y., Y. C. and Y.-c. K. C.-W. discussed sample preparation for HXN experiment; C. Z. prepared HXN sample. X. H. and H.Y. setup XRF nano-tomography and ptychography experiment, with support from E. N. and Y. C.; C. Z., Y.-c. K. C.-W. and X. H. and H. Y. conduced XRF nanotomography and ptychography experiment at HXN beamline and reconstructed the tomographic images. X. H. provided methods and software for quantitative analysis of XRF images; C. Z. conducted quantitative analysis on STEM and XRF images. B. R. designed, commissioned and setup the BMM beamline for the XANES experiment. C. Z., C. L., Y.-c. K. C.-W. and B. R. conducted an XANES experiment at BMM beamline. B.R. provided scientific insights on XANES data interpretation. C. Z. and Y.-c. K. C.-W. wrote the manuscript, with inputs from other co-authors.

Author contribution

This material is based on work supported by the National Science Foundation under Grant No. DMR-1752839. Karen Chen-Wiegart acknowledges the support provided via the Faculty Early Career Development Program (CAREER) program and Metals and Metallic Nanostructures program of National Science Foundation. The authors acknowledge the support from CFN staff: clean room access and training was provided by Gwen Wright. We thank the HXN beamline support at NSLS-II provided by Yan He, Michael Maklary and James Biancarosa. Chen-Wiegart group members are acknowledged for conducting the HXN beamtime experiment together and

assisting with preliminary analysis: Cheng-Hung Lin, Xiaoyang Liu, Yu-Chung Lin, Lijie Zou. The authors also thank Arthur Ronne for proof-reading the manuscript.

This research used resources, HXN (3-ID) and BMM (6-BM) beamlines, of the National Synchrotron Light Source II, a US Department of Energy (DOE) Office of Science User Facility operated for the DOE Office of Science by Brookhaven National Laboratory under Contract No. DE-SC0012704. This research used resources of the Center for Functional Nanomaterials, which is a U.S. DOE Office of Science Facility, at Brookhaven National Laboratory under Contract No. DE-SC0012704. Karen Chen-Wiegart, Chonghang Zhao and Cheng-Hung Lin acknowledge the financial support by the Department of Materials Science and Chemical Engineering, the College of Engineering and Applied Sciences, and the Stony Brook University, as well as by the Brookhaven National Laboratory. Chonghang Zhao and Karen Chen-Wiegart are grateful for the support of a student fellowship by the Joint Photon Science Institute at Stony Brook University, jointly proposed by Karen Chen-Wiegart as PI and Yong Chu as co-PI and Juergen Thieme and Wah-Keat Lee as collaborators.

Competing financial interests

The authors declare no competing financial interests.